ALMA CO Observations of Gamma-Ray Supernova Remnant N132D in the Large Magellanic Cloud

Possible Evidence for Shocked Molecular Clouds Illuminated by Cosmic-Ray Protons

Sano, H.; Plucinsky, P.P.; Bamba, A.; Sharda, P.; Filipović, M.D.; Law, C.J.; Alsaberi, R.Z.E.; Yamane, Y.; Tokuda, K.; Acero, F.; Sasaki, M.; Vink, J.; Inoue, T.; Inutsuka, S.; Shimoda, J.; Tsuge, K.; Fujii, K.; Voisin, F.; Maxted, N.; Rowell, G.; Onishi, T.; Kawamura, A.; Mizuno, N.; Yamamoto, H.; Tachihara, K.; Fukui, Y.

DOI
10.3847/1538-4357/abb469

Publication date
2020

Document Version
Final published version

Published in
Astrophysical Journal

The Astrophysical Journal, 902:53 (14pp), 2020 October 10 https://doi.org/10.3847/1538-4357/abb469

ALMA CO Observations of Gamma-Ray Supernova Remnant N132D in the Large Magellanic Cloud: Possible Evidence for Shocked Molecular Clouds Illuminated by Cosmic-Ray Protons

H. Sano[1,2,3], P. P. Plucinsky[4], A. Bamba[5,6], P. Sharda[7,8], M. D. Filipović[9], C. J. Law[4], R. Z. E. Alsaberi[9], Y. Yamane[2], K. Tokuda[1,10], F. Acero[11], M. Sasaki[12], J. Vink[13], T. Inoue[2], S. Inutsuka[2], J. Shimoda[2], K. Tsuge[2], K. Fujii[5], F. Voisin[14], N. Maxted[15], G. Rowell[14], T. Onishi[10], A. Kawamura[1], N. Mizuno[1], H. Yamamoto[2], K. Tachihara[2], and Y. Fukui[2,3]

[1] National Astronomical Observatory of Japan, Mitaka, Tokyo 181-8588, Japan; hidetoshi.sano@nao.ac.jp
[2] Department of Physics, Nagoya University, Furo-cho, Chikusa-ku, Nagoya 464-8601, Japan
[3] Institute for Advanced Research, Nagoya University, Furo-cho, Chikusa-ku, Nagoya 464-8601, Japan
[4] Center for Astrophysics | Harvard & Smithsonian, 60 Garden St., Cambridge, MA 02138, USA
[5] Department of Physics, Graduate School of Science, The University of Tokyo, 7-3-1 Hongo, Bunkyo-ku, Tokyo 113-0033, Japan
[6] Research Center for the Early Universe, School of Science, The University of Tokyo, 7-3-1 Hongo, Bunkyo-ku, Tokyo 113-0033, Japan
[7] Research School of Astronomy and Astrophysics, Australian National University, Canberra, ACT 2611, Australia
[8] Australian Research Council Centre of Excellence for All Sky Astrophysics in 3 Dimensions (ASTRO 3D), Australia
[9] Western Sydney University, Locked Bag 1797, Penrith South DC, NSW 1797, Australia
[10] Department of Physical Science, Graduate School of Science, Osaka Prefecture University, 1-1 Gakuen-cho, Naka-ku, Sakai 599-8531, Japan
[11] Service dAstrophysique, CEA Saclay, F-91191 Gif-sur-Yvette Cedex, France
[12] Dr. Karl Remeis-Sternwarte, Erlangen Centre for Astroparticle Physics, Friedrich-Alexander-Universität Erlangen-Nürnberg, Sternwartstraße 7, D-96049 Bamberg, Germany
[13] Anton Pannekoek Institute/GRAPPA, University of Amsterdam, P.O. Box 94249, 1090 GE Amsterdam, The Netherlands
[14] School of Physical Sciences, The University of Adelaide, North Terrace, Adelaide, SA 5005, Australia
[15] School of Science, University of New South Wales, Australian Defence Force Academy, Canberra, ACT 2600, Australia
Received 2020 July 14; revised 2020 August 30; accepted 2020 August 31; published 2020 October 12

Abstract

N132D is the brightest gamma-ray supernova remnant (SNR) in the Large Magellanic Cloud (LMC). We carried out ^{12}CO($J = 1$–0, 3–2) observations toward the SNR using the Atacama Large Millimeter/submillimeter Array (ALMA) and Atacama Submillimeter Telescope Experiment. We find diffuse CO emission not only at the southern edge of the SNR as previously known, but also inside the X-ray shell. We spatially resolved nine molecular clouds using ALMA with an angular resolution of 5″, corresponding to a spatial resolution of ∼1 pc at the distance of the LMC. Typical cloud sizes and masses are ∼2.0 pc and ∼100 $M_{\odot}$, respectively. High intensity ratios of CO $J = 3$–2/1–0 > 1.5 are seen toward the molecular clouds, indicating that shock heating has occurred. Spatially resolved X-ray spectroscopy reveals that thermal X-rays in the center of N132D are produced not only behind a molecular cloud but also in front of it. Considering the absence of a thermal component associated with the forward shock toward one molecular cloud located along the line of sight to the center of the remnant, this suggests that this particular cloud is engulfed by shock waves and is positioned on the near side of the remnant. If the hadronic process is the dominant contributor to the gamma-ray emission, the shock-engulfed clouds play a role as targets for cosmic rays. We estimate the total energy of cosmic-ray protons accelerated in N132D to be ∼0.5–3.8 $\times$ 10^{49} erg as a conservative lower limit, which is similar to that observed in Galactic gamma-ray SNRs.

Unified Astronomy Thesaurus concepts: Supernova remnants (1667); Interstellar medium (847); Cosmic-ray sources (328); Gamma-ray sources (633); X-ray sources (1822); Large Magellanic Cloud (903)

1. Introduction

It has been a long-standing question how cosmic rays, consisting of mainly relativistic protons, are accelerated in interstellar space. Supernova remnants (SNRs) are promising candidates for acceleration sites of Galactic cosmic rays below the knee energy (∼3 $\times$ 10^{15} eV), through the mechanism of diffusive shock acceleration (DSA; e.g., Bell 1978; Blandford & Ostriker 1978) at their shocks. A conventional value of the total energy of Galactic cosmic rays accelerated in an SNR is thought to be ∼10^{49}–10^{50} erg, corresponding to ∼1%–10% of the typical kinematic energy released by a supernova explosion (10^{51} erg; e.g., Leahy et al. 2019). One of the current challenges is to verify these predictions experimentally.

A young SNR (a few thousand years old) with bright teraelectronvolt gamma-ray emission is a potential source for accelerating cosmic rays close to knee energy (see Ohira et al. 2012; Funk 2015; Bykov et al. 2018). Teraelectronvolt gamma rays from young SNRs can be generally produced by two different mechanisms: hadronic and leptonic processes (e.g., Fazio 1967; Stecker 1971; Dermer 1986). For the hadronic process, interaction between a cosmic-ray proton and an interstellar proton creates a neutral pion that decays into two gamma-ray photons (referred to as "hadronic gamma rays"). For the leptonic process, a cosmic-ray electron energizes an interstellar photon to gamma-ray energy via inverse Compton scattering (refer to as "leptonic gamma rays"). To establish the SNR origin of cosmic-ray protons, an observational detection of hadronic gamma rays is needed. However, it is difficult to distinguish the hadronic/leptonic processes from spectral modeling alone (e.g., Inoue et al. 2012; H.E.S.S. Collaboration et al. 2018c, 2018a, 2018b).

Investigating the interstellar gas associated with gamma-ray SNRs holds a key to solving this problem. If the hadronic process dominates, the gamma-ray flux is proportional to the number density of the interstellar gas assuming an azimuthally isotropic distribution of cosmic rays. This implies that the presence of gamma rays should be spatially coincident with the interstellar gas. Fukui et al. (2012) demonstrated the spatial correspondence using CO/H I data sets as interstellar molecular and atomic gas tracers and teraelectronvolt gamma-ray data toward the Galactic SNR RX J1713.7−3946. The authors also derived the total energy of cosmic rays to be $\sim 10^{48}$ erg by adopting the number density of interstellar gas that interacts with the SNR. Subsequent studies toward the young teraelectronvolt gamma-ray SNRs HESS J1731−347, Vela Jr., and RCW 86 in the Milky Way show similar values of $\sim 10^{48}$–10^{49} erg (e.g., Fukuda et al. 2014; Fukui et al. 2017; Sano et al. 2019c). To better understand the origin of cosmic rays and their energy budget, we need to study not only Galactic SNRs, but also extragalactic sources such as gamma-ray-bright SNRs in the nearby Large Magellanic Cloud (LMC) and the Small Magellanic Cloud (SMC).

2. Overview of the Magellanic SNR N132D

N132D (LHA 120-N 132D) is the brightest X-ray and teraelectronvolt gamma-ray SNR in the LMC (e.g., H.E.S.S. Collaboration et al. 2015; Maggi et al. 2016; Martin et al. 2019). The shell-like morphology of this remnant is clearly resolved in radio, infrared, optical, and X-ray wavelengths (e.g., Dickel & Milne 1995; Morse et al. 1996; Tappe et al. 2006; Borkowski et al. 2007), with a size of $114'' \times 90''$[16] or ∼25 pc at the distance of the LMC (50 ± 1.3 kpc, Pietrzyński et al. 2013). The age of the SNR is estimated to be ∼2500 yr (Morse et al. 1995; Hughes et al. 1998; Vogt & Dopita 2011; Law et al. 2020). N132D is also categorized as an oxygen-rich (or O-rich) SNR, which most likely originated from a core-collapse supernova explosion (e.g., Danziger & Dennefeld 1976; Lasker 1978; Hughes 1987; Blair et al. 2000; Sharda et al. 2020). Detailed optical studies revealed kinematic motions of O-rich ejecta using Doppler reconstructions with an average expansion velocity of 1745 km s^{-1} (Lasker 1980; Morse et al. 1995; France et al. 2009; Vogt & Dopita 2011; Law et al. 2020).

Since the detection of teraelectronvolt gamma-ray emission associated with N132D, it has received much attention as a possible efficient accelerator of cosmic rays. The H.E.S.S. Collaboration et al. (2015) first reported the significant detection of teraelectronvolt gamma rays toward three sources in the LMC, including the superbubble 30 Doradus C, and two SNRs N157B and N132D. The authors derived the 1–10 TeV gamma-ray luminosity of $(0.9 \pm 0.2) \times 10^{35}$ erg s^{-1} for N132D at the assumed distance of 50 kpc, which is an order of magnitude higher than that of the young (∼1600 yr) teraelectronvolt gamma-ray SNR RX J1713.7−3946 in the Galactic plane. A subsequent gigaelectronvolt gamma-ray study using Fermi-LAT reported a 1–100 GeV gamma-ray luminosity of $\sim 10^{36}$ erg s^{-1}, indicating that N132D is the brightest gigaelectronvolt gamma-ray SNR not only in the Magellanic Clouds but also in the Local Group galaxies (Acero et al. 2016; Ackermann et al. 2016). Bamba et al. (2018) discovered hard X-ray emission (E: 10–15 keV) using NuSTAR. The authors derived an upper limit on the synchrotron X-ray flux of 2.0×10^{35} erg s^{-1} in the 2–10 keV band using Suzaku and NuSTAR, and they argued that a high flux ratio of teraelectronvolt gamma rays and synchrotron X-rays is consistent with the hadronic origin of gamma rays. However, to estimate the total energy of cosmic rays, the number density of interacting molecular and atomic clouds is needed.

N132D is also believed to be associated with a giant molecular cloud (GMC) that might be a possible target for cosmic-ray protons. Banas et al. (1997) discovered a GMC toward the south of N132D using ^{12}CO($J = 2$–1) line emission with the Swedish-ESO Submillimeter Telescope (SEST). The GMC has a size of ∼22 pc and a virial mass of at least $\sim 2 \times 10^5\ M_\odot$. The authors suggested that part of the GMC is interacting with the southern edge of the SNR. This interpretation was further supported by the presence of shock-heated dust components in the southeastern shell of N132D (e.g., Williams et al. 2006; Tappe et al. 2006, 2012; Seok et al. 2013; Dopita et al. 2018; Zhu et al. 2019). Subsequently, Desai et al. (2010) and Sano et al. (2015b) presented a CO map using archival ^{12}CO($J = 1$–0) line emission data that was taken by the Mopra 22 m radio telescope as part of the Magellanic Mopra Assessment project (MAGMA; Wong et al. 2011). A diffuse part of the GMC is possibly aligned with the southern shell of the SNR, while no dense clouds are found inside the shell. Owing to the modest angular resolution of the CO data of ∼23″–45″ (or ∼6–11 pc at the LMC distance) and lack of higher excitation line data (e.g., ^{12}CO $J = 3$–2, 4–3), there is no conclusive evidence for shock-heated molecular clouds in the existing data of this remnant.

In this study, we report new millimeter/submillimeter observations using ^{12}CO($J = 1$–0, 3–2) line emission with the Atacama Submillimeter Telescope Experiment (ASTE) and the Atacama Large Millimeter/submillimeter Array (ALMA). The high angular resolution of 5″ in the ALMA CO data will allow us to resolve molecular clouds illuminated by shock waves and cosmic-ray protons in N132D. Section 3 gives details about the observations, data reductions, and archival data. Sections 4.1 and 4.2 show a large-scale view of the CO, H I, X-ray, and teraelectronvolt gamma-ray emission; Section 4.3 presents ALMA CO results and basic properties of the molecular clouds; Section 4.4 discusses the excitation condition of the molecular clouds; Section 4.5 gives a detailed comparison with the O-rich ejecta; and Sections 4.6 and 4.7 present X-ray spectroscopy and a comparison with hard X-ray emission. Discussion and conclusions are given in Sections 5 and 6, respectively.

3. Observations, Data Reductions, and Archival Data

3.1. CO

Observations of ^{12}CO($J = 3$–2) line emission at $\lambda = 0.87$ mm wavelength were conducted in 2014 September 1–3 (PI: H. Sano, proposal No. AC141006) using the ASTE 10 m radio telescope (Ezawa et al. 2004). The telescope is installed at an altitude of 5000 m in the Atacama Desert in Chile, operated by the Chile Observatory of the National Astronomical Observatory of Japan (NAOJ). We used the on-the-fly mapping mode with Nyquist sampling, and the effective observation area was $3.6' \times 3.6'$ centered at $(\alpha_{J2000}, \delta_{J2000}) \sim (05^h25^m2\overset{s}{.}8, -69°38'35'')$. The front end was a sideband-separating superconductor–insulator–superconductor (SIS) mixer receiver "CATS 345" (Inoue et al. 2008). We utilized an XF-type digital spectrometer "MAC" (Sorai et al. 2000) as the back end. The bandwidth of MAC is 128 MHz

[16] See also catalog papers of the LMC SNRs by Badenes et al. (2010) and Bozzetto et al. (2017).

with 1024 channels, corresponding to a spectral resolution of 0.125 MHz. The velocity coverage and resolution are thus ∼111 km s^{-1} and ∼0.11 km s^{-1}, respectively. The typical system temperature was ∼300 K, including the atmosphere in the single-side band. To derive the main beam efficiency, we observed N 159W (α_{J2000}, δ_{J2000} = 05^{h}40^{m}3.″7, −68°47′00″; Minamidani et al. 2011), obtaining a main beam efficiency of 0.67 ± 0.08. We also observed the M-type AGB star R Dor every hour to satisfy pointing offset accuracy within 2″. After convolution with a two-dimensional Gaussian kernel, we obtained the cube data with a beam size of ∼23″ (∼5.6 pc at the LMC distance). The typical noise fluctuations are ∼0.046 K at the velocity resolution of 0.4 km s^{-1}.

Observations of ^{12}CO(J = 1–0) line emission at λ = 2.6 mm wavelength were carried out using the ALMA Band 3 (86–116 GHz) in Cycle 2 as an early science project (PI: H. Sano, proposal No. 2013.1.01042.S). We utilized 40 antennas of the 12 m array, nine antennas of the 7 m array, and three antennas of the total power (TP) array. The effective observation area was a 150″ × 150″ rectangular region centered at (α_{J2000}, δ_{J2000}) ∼ (05^{h}25^{m}2.″79, −69°38′34.″2). The combined baseline length of the 12 m and 7 m arrays ranges from 7.2 to 215.7 m, corresponding to u–v distances from 2.8 to 82.9 $k\lambda$. The two quasars J0334−4008 and J0635−7516 were used for complex gain calibrators. Another two quasars J0601−7036 and J0526−6749 were observed as phase calibrators. We also observed Callisto, Uranus, and a quasar J0519-454 as flux calibrators. The data reduction was performed using the Common Astronomy Software Application (CASA; McMullin et al. 2007) package version 5.4.0. We used the *multiscale CLEAN* task implemented in the CASA package (Cornwell 2008). The scale parameters are 0″, 3.″18, and 9.″54 for the 12 m array and 0″, 14.″64, and 43.″92 for the 7 m array. To improve the imaging quality, we also applied a *uvtaper* during the clean procedure for the 12 m array data. The u–v tapering applies a multiplicative Gaussian taper to the spatial frequency space to downweight high spatial frequencies. This can suppress artifacts—for example, strong side lobes—arising from poorly sampled areas near and beyond the maximum spatial frequency. We finally combined the cleaned data of the 12 and 7 m array data sets and calibrated the TP array data by using the *feather* task. The final beam size of the feathered data is 5.″26 × 4.″99, with a position angle of 59.°60, corresponding to a spatial resolution of ∼1.2 pc at the LMC distance. The typical noise fluctuations of the feathered data are ∼0.22 K at a velocity resolution of 0.4 km s^{-1}.

To investigate the CO gas distribution at larger spatial scales, we used the Magellanic Mopra Assessment Data Release 1 (MAGMA DR1, Wong et al. 2011). MAGMA is a ^{12}CO(J = 1–0) mapping survey of the LMC using the Mopra 22 m radio telescope of the Australia Telescope National Facility (ATNF). The angular resolution is 45″, corresponding to the spatial resolution of ∼11 pc at the LMC distance. The typical noise fluctuations of a region surrounding N132D are ∼0.26 K at the velocity resolution of 0.53 km s^{-1}. We applied additional spatial smoothing with a two-dimensional Gaussian kernel. The angular resolution of the smoothed data is ∼60″ (∼15 pc at the LMC distance), which is the same resolution as for the H I survey data of the LMC (see Section 3.2).

3.2. H I

To better understand the distribution of neutral atomic hydrogen toward N132D, we used archival survey data of the H I line at λ = 21 cm wavelength published by Kim et al. (2003). The survey data were obtained using the Australia Telescope Compact Array (ATCA) and Parkes 64 m telescopes operated by ATNF. The angular resolution of the survey data is 60″, corresponding to the spatial resolution of ∼15 pc at the LMC distance. The typical noise fluctuations of brightness temperature are ∼2.4 K at the velocity resolution of 1.689 km s^{-1}.

Table 1
Chandra ACIS-S Observation Log of SNR N132D

ObsID	Observation Date	Exposure (ks)	α_{J2000} (^{h} ^{m} ^{s})	δ_{J2000} (° ′ ″)
05532	2006 Jan 09	44.59	05 25 02.28	−69 38 37.32
07259	2006 Jan 10	24.85	05 25 02.28	−69 38 37.32
07266	2006 Jan 15	19.90	05 25 02.28	−69 38 37.32

3.3. X-Rays

We used archival X-ray data obtained by Chandra, for which the observation IDs are 5532, 7259, and 7266 (PI: K. J. Borkowski, proposal No. 06500305), which have been published in previous papers (e.g., Borkowski et al. 2007; Xiao & Chen 2008; Schenck et al. 2016; Sharda et al. 2020). The data sets were taken with the Advanced CCD Imaging Spectrometer S-array (ACIS-S3). Table 1 lists the details of the observations. We utilized Chandra Interactive Analysis of Observations (CIAO, Fruscione et al. 2006) software version 4.12 with CALDB 4.9.1 (Graessle et al. 2007) for data reduction. All of the data sets were reprocessed using the *chandra_repro* task. We then created exposure-corrected, energy-filtered images using the *fluximage* task in the energy bands 0.35–0.85 keV, 0.5–1.2 keV (soft band), 0.85–1.6 keV, 1.2–2.0 keV (medium band), 1.6–6.0 keV, 2.0–7.0 keV (hard band), and 0.5–7.0 keV (broad band). The total effective exposure is ∼89.3 ks. For the spectral analysis, we used HEASOFT (version 6.25), including spectral fitting with XSPEC (version 12.10.1f, Arnaud 1996). We fit the spectra in the energy band 0.3–10.0 keV, and the errors of the fitted parameters are quoted at the 1σ confidence level unless specified otherwise. We fit the unbinned spectra to preserve the maximum spectral information. Following Sharda et al. (2020), we explicitly model the background as opposed to subtracting it. We use the C statistic (Cash 1979) as the minimization statistic to avoid the well-known bias introduced by the χ^2 statistic in the case of a low number of counts per spectral bin (Kaastra 2017), and we report the Pearson χ^2 (weighting by the model) to evaluate goodness of fit. We used ATOMDB version 3.0.9 (Foster et al. 2013) and nonequilibrium ionization (NEI) version 3.0.4 for the NEI models (Borkowski et al. 2001). We used the cosmic abundance given by Wilms et al. (2000) as the baseline abundance for all our analysis and the cross sections given by Verner et al. (1996).

To investigate the origin of the hard X-ray emission in N132D, we also used a map of the hard-band X-ray (E: 10–15 keV) obtained with NuSTAR (Bamba et al. 2018). The NuSTAR observations were executed on 2015 December 10–11. The total effective exposure is 62.3 ks. The angular resolution is 18″ (half-power beam width, HPBW) or 58″ (half-power diameter, HPD). To improve the signal-to-noise ratios of the map, we smoothed the data with a two-dimensional Gaussian kernel of 20″.

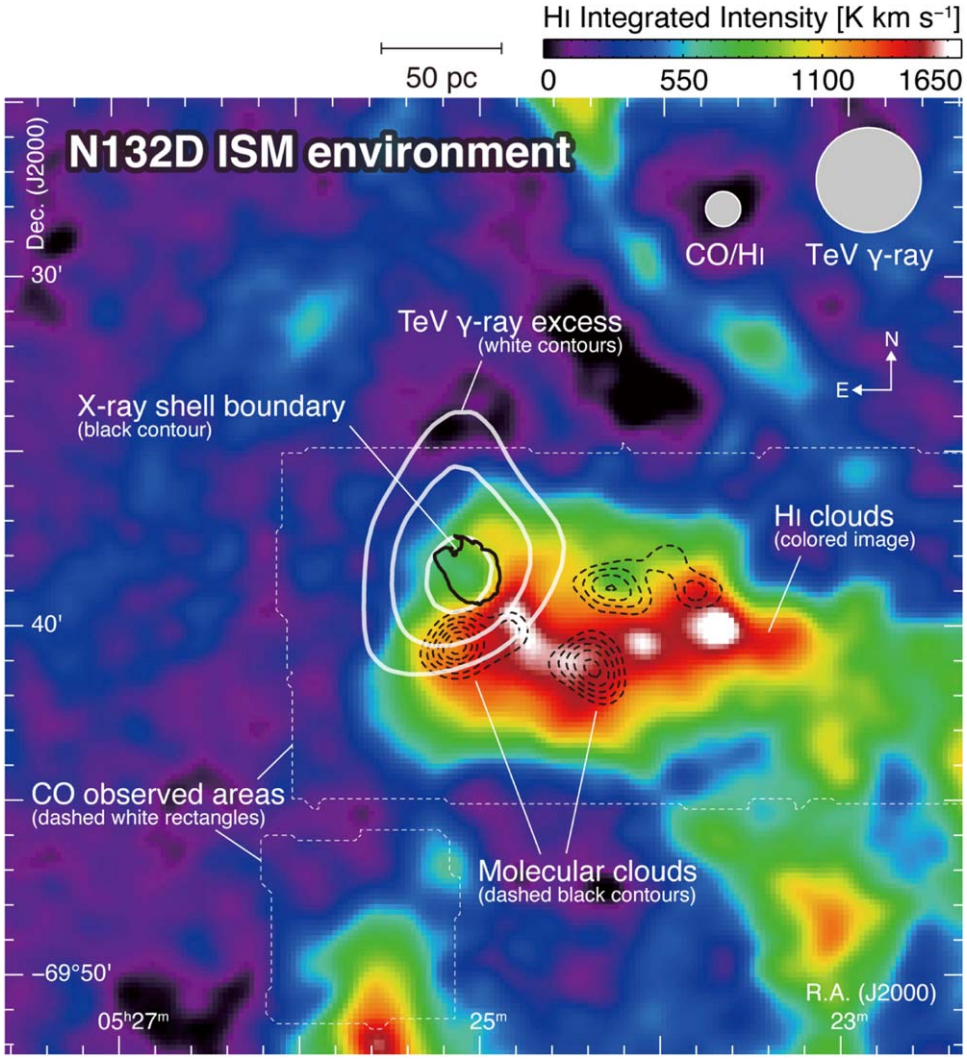

Figure 1. Integrated intensity map of the ATCA and Parkes H I (Kim et al. 2003, colored image) overlaid with the Mopra ^{12}CO(J = 1–0) integrated intensity (black dashed contours), Chandra X-ray boundary of N132D (Borkowski et al. 2007, black solid contour), and the H.E.S.S. teraelectronvolt gamma-ray excess counts (H.E.S.S. Collaboration et al. 2015, white solid contours). The CO data have been spatially smoothed to match the FWHM of H I (∼60″). The integration velocity ranges of CO and H I are from 240 to 290 km s^{-1}, which cover 74% of the total integrated intensity of H I. The lowest contour level and intervals of CO are 6.3 K km s^{-1} (∼9σ) and 2.1 K km s^{-1} (∼3σ), respectively. The contour level of the X-ray boundary is 0.3 × 10^{-6} counts pixel^{-1} s^{-1}. The contour levels of teraelectronvolt gamma rays are 10, 14, and 18 excess counts. The dashed white rectangles indicate the observed areas of CO. The FWHM beam size of CO/H I and the PSF of the teraelectronvolt gamma rays are also shown in the top right corner.

3.4. Teraelectronvolt Gamma Rays

To compare the spatial distribution with the interstellar medium (ISM) environment of N132D, we also used an excess count map of teraelectronvolt gamma rays obtained by the High Energy Stereoscopic System (H.E.S.S. Collaboration et al. 2015). The angular resolution is ∼3′ for the point-spread function (PSF, 68% containing radius) or ∼7′ for the FWHM, corresponding to a spatial resolution of ∼44 pc for the PSF or ∼100 pc for the FWHM.

3.5. Hα and [O III]

The optical data of the Hα and [O III] emission lines are used to derive the spatial distributions of the ionized gas and shocked ejecta. We utilized the Hubble Space Telescope (HST) Wide Field Planetary Camera 2 (WFPC2) and the Advanced Camera for Survey (ACS) images from the Hubble Legacy Archive.[17] The observations were carried out using the ACS Wide Field Channel F658N for Hα and the WFPC2 F502N for [O III], which have been published by Morse et al. (1996) and Borkowski et al. (2007). For further details about the data reductions and pipeline processes, we refer the reader to the HST Data Handbook.[18]

4. Results

4.1. Large-scale Distribution of CO, H I, X-Rays, and Teraelectronvolt Gamma Rays

Figure 1 shows a map of ATCA and Parkes H I intensity overlaid with the Mopra ^{12}CO(J = 1–0) intensity (black dashed contours), Chandra X-ray boundary of N132D (black solid contours), and the H.E.S.S. teraelectronvolt gamma rays (white solid contours). An H I cloud appears projected onto the SNR that is elongated to the southwest direction with a hollow

[17] hla.stsci.edu

[18] www.stsci.edu/hst/HST_overview/documents/datahandbook

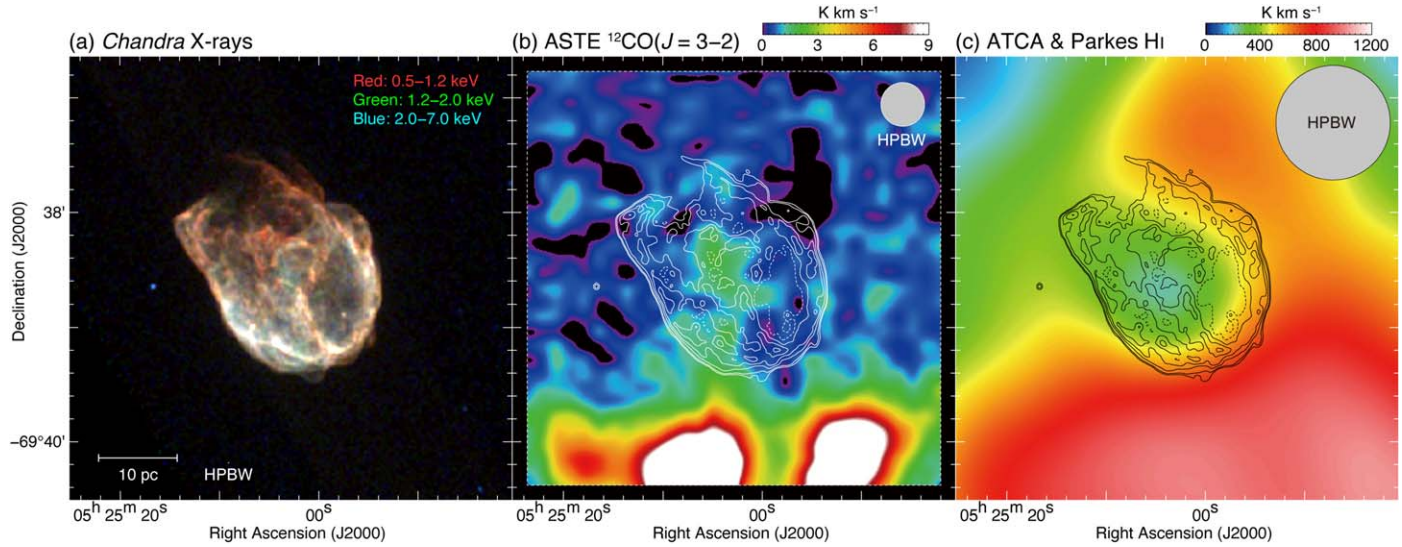

Figure 2. (a) RGB X-ray image of N132D obtained with Chandra (e.g., Borkowski et al. 2007; Xiao & Chen 2008; Sharda et al. 2020). The red, green, and blue colors represent the energy bands 0.5–1.2 keV, 1.2–2.0 keV, and 2.0–7.0 keV, respectively. (b) Intensity map of ^{12}CO(J = 3–2) obtained with ASTE overlaid with the Chandra X-ray contours. The integration velocity range is from 256.8 km s^{-1} to 271.2 km s^{-1}. The black contours represent the X-ray intensities: 0.3, 0.6, 1.8, 3.6, 7.2, and 14.4 × 10^{-6} counts pixel^{-1} s^{-1}. (c) Intensity map of H I obtained with ATCA and Parkes (Kim et al. 2003) overlaid with the Chandra X-ray contours. The integration velocity range and contour levels are the same as in Figure 2(b). The beam size and scale bar are also shown.

structure along the X-ray shell boundary. Three to four GMCs are located near the local intensity peaks of the H I cloud. One of them is possibly associated with the southern shell boundary of the SNR, which is consistent with previous CO studies (Banas et al. 1997; Desai et al. 2010; Sano et al. 2015b). Note that there are no dense molecular and atomic clouds toward the northeast outside the SNR. Further, note that teraelectronvolt gamma rays are emitted from the SNR itself rather than from the surrounding GMCs and H I cloud, even after taking into consideration the large PSF of the gamma-ray data.

4.2. CO and H I Clouds toward the SNR

Figure 2(a) shows a red/green/blue (RGB) image of N132D obtained with Chandra. The X-ray shell shows an incomplete elliptical morphology, slightly elongated in the southwestern direction, with a breakout structure in the northeast. Many filamentary structures of X-rays appear not only in the shell boundary but also inside the SNR. The hard-band X-rays (E: 2.0–7.0 keV) are brighter in the southeastern shell.

Figures 2(b) and (c) show the integrated intensity maps of ASTE ^{12}CO(J = 3–2) and ATCA and Parkes H I. Using high-sensitivity and full-spatial-sampling observations of CO line emission, we found a molecular cloud toward the center of the SNR (hereafter "N132D MC-center"). Note that N132D MC-center is significantly detected because the CO integrated intensity of 1.12 K km s^{-1} represents the ∼10σ level. The spatially resolved MC-center cloud is more extended than the beam size, with 10σ or higher significance in integrated intensity. We also confirm the presence of the previously identified GMC (hereafter "N132D GMC-south") in contact with the southeastern edge of the SNR. The peak velocities of the clouds are $V_{\rm LSR}$ ∼ 264 km s^{-1} for N132D MC-center and $V_{\rm LSR}$ ∼ 266 km s^{-1} for N132D GMC-south, and the latter is roughly consistent with the previous CO observations using SEST (Banas et al. 1997). On the other hand, the overall distribution of H I tends to encircle the X-ray shell except for northeast at the same velocity range of CO ($V_{\rm LSR}$ = 256.8–271.2 km s^{-1}). We also find that diffuse H I gas with an intensity of ∼300 K km s^{-1} fills the interior of the X-ray shell.

Figure 3 shows a position–velocity diagram of CO and H I. We find an intensity dip at the velocity of ∼266 km s^{-1}, which is roughly centered at the position of the SNR in decl. On the other hand, the CO clouds appear projected onto the edge of the H I dip at the intensity level of 0.3 K degree (dashed contour centered at ∼266 km s^{-1}). Figure 4 shows averaged line profiles of CO and H I. The velocity range of the H I cloud at $V_{\rm LSR}$ ∼ 250–280 km s^{-1} contains that of CO clouds at $V_{\rm LSR}$ ∼ 260–270 km s^{-1}. A strong absorption line of H I is detected at the velocity of $V_{\rm LSR}$ ∼ 266 km s^{-1} toward only the SNR direction (blue, inside the SNR), suggesting that the absorption line was caused by the proximity of strong radio continuum radiation from the SNR (Yamane et al. 2018; Sano et al. 2018, 2019a). We therefore focus on both the CO and H I clouds around $V_{\rm LSR}$ ∼ 266 km s^{-1} that are likely related to the SNR.

4.3. Detailed CO Distribution with ALMA

Figure 5 shows an RGB image of N132D composed of a combination of *HST* Hα (red), ALMA ^{12}CO(J = 1–0) integrated intensity (green), and Chandra broadband X-rays (blue). We spatially resolved nine molecular clouds, named A to I, within the X-ray shell of N132D. Cloud A is located in the breakout region with very faint X-rays. Clouds H and I lie on the edge of the southwestern shell. The other clouds, B to G, corresponding to N132D MC-center, are concentrated in the center of the SNR. In other words, N132D MC-center is split into clouds B to G owing to high-resolution observations using ALMA. Note that clouds B, C, E, and F are located in the vicinity of Hα blobs or filaments, as shown in red.

To derive the masses of these molecular clouds, we utilize the following equations:

$$M = m_{\rm p}\mu\Omega D^2 \sum_i N_i({\rm H}_2), \quad (1)$$

$$N({\rm H}_2) = A \cdot W[^{12}{\rm CO}(J = 1 - 0)], \quad (2)$$

where $m_{\rm p}$ is the mass of atomic hydrogen, μ = 2.72 is the mean molecular weight, Ω is the solid angle of each data pixel,

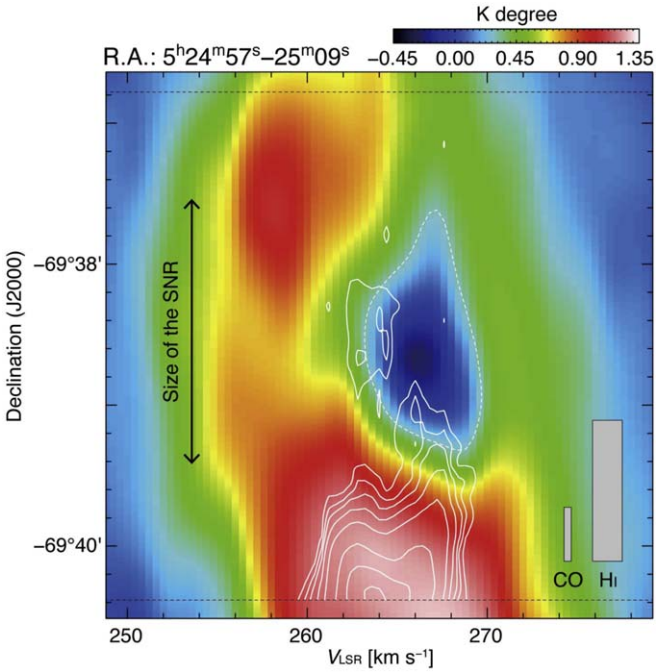

Figure 3. Position–velocity diagram of H I. Superposed white solid contours indicate ^{12}CO(J = 3–2) intensity. The integration range in R.A. is from $05^h24^m57^s$ to $05^h25^m09^s$. The lowest contour and contour intervals of CO are 0.003 K degree and 0.005 K degree, respectively. The dashed white line delineates an H I cavity with the H I intensity of 0.3 K degree. The beam size and velocity resolution are also shown in the bottom right corner. Horizontal dashed lines represent observed boundaries of CO.

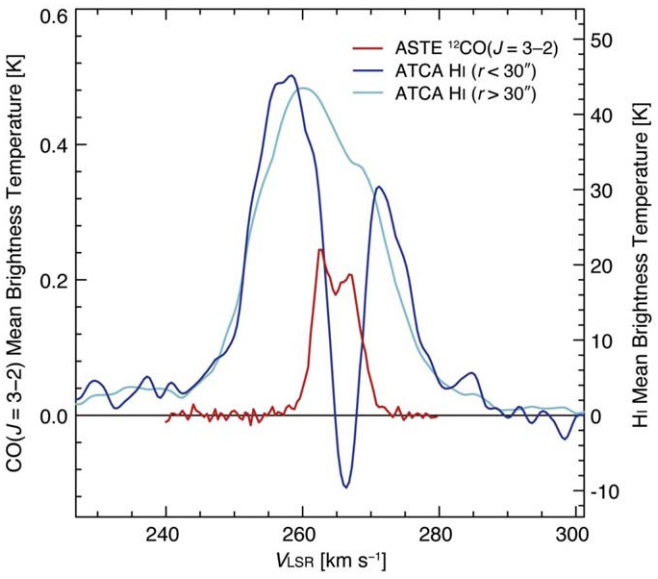

Figure 4. Averaged line profiles of ^{12}CO(J = 3–2) (red) and H I (blue and cyan) toward the SNR N132D. The blue and cyan spectra were extracted from regions inside and outside a circle with radius 30″ at the center position of (α_{J2000}, δ_{J2000}) ∼ ($05^h25^m02^s.88$, −69°38′34.″8). The red spectrum was produced by averaging the whole spectra shown in Figure 2(b).

D is the distance to the LMC (=50 kpc), $N_i(H_2)$ is the column density of molecular hydrogen for each data pixel i, A is the CO-to-H_2 conversion factor, and $W[^{12}CO(J = 1 - 0)]$ is the integrated intensity of ^{12}CO(J = 1–0) line emission. Here, we use the CO-to-H_2 conversion factor $A = 7.0 \times 10^{20}$ cm^{-2} (K km s^{-1})$^{-1}$ (Fukui et al. 2008). The size of each molecular cloud is defined as an effective diameter, determined by the contour of the half-level of maximum integrated intensity. The detailed definitions and physical properties of molecular clouds are summarized in Table 2. The typical cloud masses and sizes are ∼50–100 $M_\odot$ and ∼1.5–2.0 pc, respectively. Note that the mass, $n(H_2)$, and size of each cloud have ∼30% relative errors, due to uncertainties in the CO-to-H_2 conversion factor and distance to the LMC. There are no broad-line features with a velocity width more than 10 km s^{-1}, whereas the line widths of cloud A ($\Delta V = 5.7$ km s^{-1}) and cloud B ($\Delta V = 4.4$ km s^{-1}) are significantly larger than that of the other clouds ($\Delta V \sim$ 1–2 km s^{-1}).

4.4. CO 3–2/1–0 Ratio

Figure 6 shows an intensity ratio map of ^{12}CO(J = 3–2)/^{12}CO(J = 1–0) (hereafter $R_{3-2/1-0}$) using ASTE and ALMA, overlaid with Chandra X-ray contours. The intensity ratio reflects the CO rotational excitation states of the molecular clouds, and hence a high intensity ratio $R_{3-2/1-0}$ indicates a high temperature of the cloud. We find a high intensity ratio $R_{3-2/1-0}$ of ∼1.5–2.0 within the X-ray shell boundary. On the other hand, the intensity ratio $R_{3-2/1-0}$ of N132D GMC-south, south of the SNR, is ∼0.4, corresponding to the typical values of quiescent molecular clouds without any embedded OB association or shocks (e.g., Celis Peña et al. 2019).

4.5. Comparison with O-rich Ejecta

Figure 7(a) shows an enlarged view of the central region of N132D containing molecular clouds (green contours) and O-rich ejecta as seen by optical [O III] emission (red) and O VII plus O VIII images of X-rays (blue, see the Appendix and Figure 11). The optical [O III] emission is especially bright toward clouds B and C, also known as Lasker's Bowl (Morse et al. 1996). The intercloud region between clouds D and F is also bright in both the [O III] and O VII plus O VIII emission, whereas no bright O-rich ejecta is detected toward the center of cloud F. We find no apparent trend between the spatial distributions of the molecular clouds and O-rich ejecta. Figure 7(b) shows radial velocity distributions of the O-rich knots presented by Law et al. (2020), overlaid with the ALMA CO contours. Major O-rich knots—B1, B2, B3, B4, R1, R2, and RK (runaway knot)—defined by Morse et al. (1995) are also indicated. We find that clouds B to F are projected onto the O-rich knots; cloud E is in contact with the blueshifted O-rich knots, whereas clouds B to D lie in the redshifted O-rich knots. Cloud F is possibly associated with both the blue and redshifted O-rich knots. It is noteworthy that cloud F shows a good spatial coincidence with the kinematic center of O-rich knots (marked with star symbol). Note that there are no CO counterparts of B1 and RK.

4.6. X-Ray Spectral Analysis

To investigate the relationship between the molecular clouds and the X-ray emission of N132D, we derive the absorbing column densities toward two regions: one at the position of cloud F, and the other at a reference position south of cloud F (see Figure 7(a)). The absorbing column density is useful for constraining the origin of the X-ray emission. This might provide evidence for a possible positional relationship between

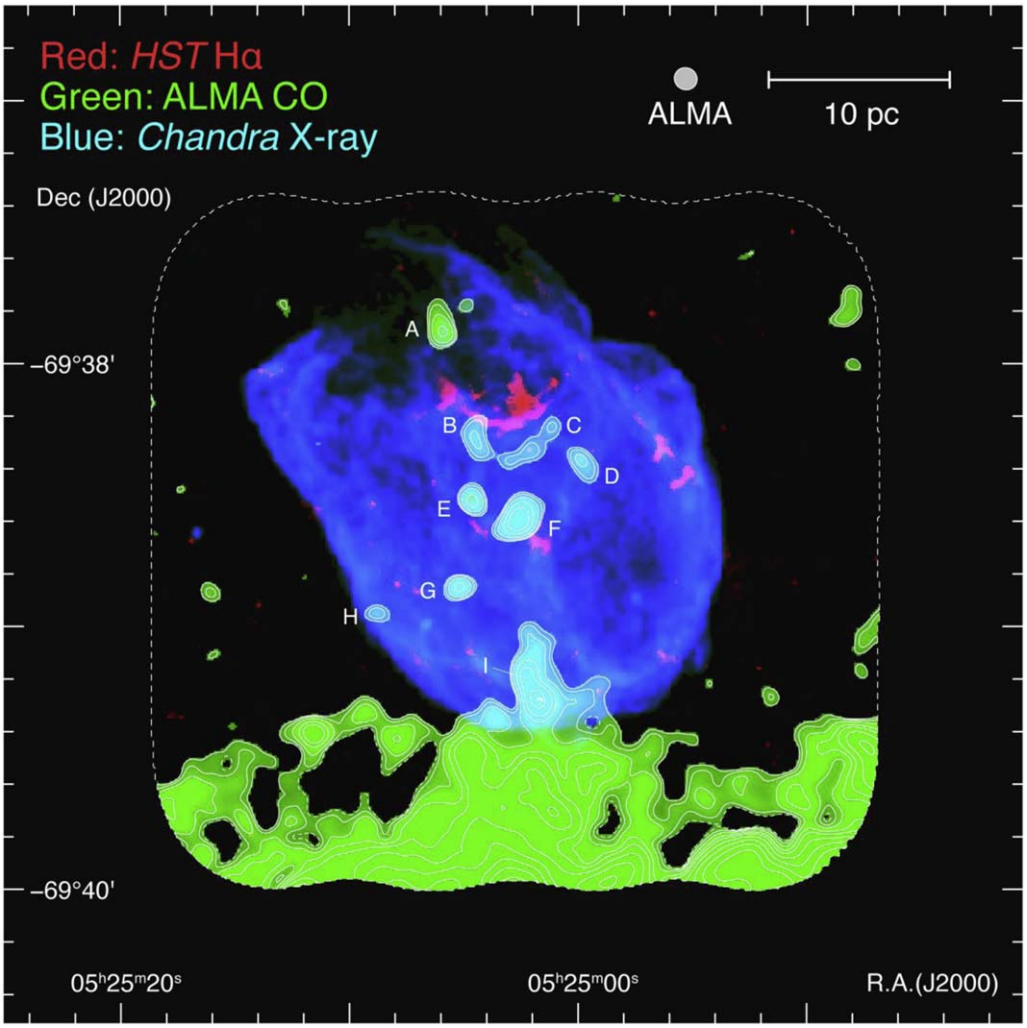

Figure 5. RGB image of N132D obtained with the *HST* Hα (red), ALMA ^{12}CO(J = 1–0) (green), and Chandra X-rays in the energy band 0.5–7.0 keV (blue). The integration velocity range is from 262.0 km s^{-1} to 268.4 km s^{-1}. The contours represent the integrated intensity of CO, whose levels are 1.2 ($\sim 3\sigma$), 1.5, 2.0, 3.0, 4.0, 6.0, 9.0, 13.0, 18.0, and 24.0 K km s^{-1}. The region enclosed by the dashed line indicates the area observed with ALMA. The CO clouds, named A to I, discussed in Section 4.3 are indicated.

the cloud and the shock front (Sano et al. 2015a, 2019a; Y. Yamane et al. submitted to ApJ).

We extracted ACIS-S3 spectra from the regions labeled as the "center region" and "southwest region" in Figure 7(a). We extracted the background spectrum from two rectangular regions with a total area of 2.8 arcmin^2 to provide sufficient statistics. One region was located to the southwest of the remnant and the other to the northeast; both were positioned to include the contribution from the transfer streak of the CCD. We use the background model of Sharda et al. (2020) to fit both the source and the background spectra for each region.

We used a two-component absorption model composed of the Milky Way absorption $N_{\rm H,MW}$ (TBabs) and the LMC absorption $N_{\rm H,LMC}$ (TBvarabs) by the ISM within the LMC along the line of sight. We fixed the hydrogen column density of the Milky Way at 1.47×10^{21} cm^{-2} (HI4PI Collaboration et al. 2016) with solar abundance (Wilms et al. 2000). Further, we set the elemental abundance for the ISM in the LMC with He = 0.9 $Z_\odot$ and the other elements at 0.5 $Z_\odot$ on the Wilms et al. (2000) scale.

Following the latest X-ray study of N132D (Sharda et al. 2020), we fitted each source spectrum with a plane-parallel shock model (`vpshock`, see Borkowski et al. 2001) plus two NEI components (`vnei` + `vnei`). The thermal emission from the forward shock along the outer rim has been modeled by Sharda et al. (2020) with a `vpshock` model with a temperature of $kT_{\rm e} = 0.86$ keV and an ionization timescale of 1.94×10^{11} cm^{-3} s. We fix these parameters at these values in our fits and only allow the normalization to vary. The `vpshock` component is intended to represent any emission from the forward shock that may contribute to our spectra along the line of sight. The two `vnei` components are intended to represent emission from a shock/cloud interface or shock-heated ejecta.

Figure 8 and Table 3 show the spectral fit results and the best-fit parameters, respectively. For the center region (cloud F), the C statistic is 1350 with 1302 degrees of freedom (DOF), and the Pearson reduced χ^2 is 0.99. The normalization of the `vpshock` component went to 0.0, and the LMC absorption went to $1.03 \pm 0.10 \times 10^{21}$ cm^{-2}. One `vnei` component goes to a moderate temperature ($\sim$0.82 keV) and has the abundances of O, Ne, Mg, Si, S, and Fe free to vary. There is marginal evidence for enhanced O, Ne, Mg, Si, and S abundances, but the Fe abundance is consistent with LMC values. The other `vnei` goes to a high temperature (3.36 keV) and has

Table 2
Physical Properties of Molecular Clouds Associated with N132D

Cloud Name	α_{J2000} ($^h\ ^m\ ^s$)	δ_{J2000} ($^\circ\ '\ ''$)	T_{mb} (K)	V_{LSR} (km s^{-1})	ΔV (km s^{-1})	Size (pc)	Mass ($M_\odot$)	$n(H_2)$ (cm^{-3})
(1)	(2)	(3)	(4)	(5)	(6)	(7)	(8)	(9)
A	05 25 05.94	−69 37 52.9	0.79 ± 0.08	263.5 ± 0.3	5.7 ± 0.7	1.6	90	910
B	05 25 04.42	−69 38 17.8	0.52 ± 0.09	263.5 ± 0.4	4.4 ± 0.9	1.8	70	450
C	05 25 01.17	−69 38 14.1	0.74 ± 0.18	263.6 ± 0.1	1.1 ± 0.3	2.2	40	130
D	05 24 59.95	−69 38 22.1	1.34 ± 0.15	262.6 ± 0.1	1.5 ± 0.2	1.7	50	410
E	05 25 04.62	−69 38 31.6	1.86 ± 0.12	264.1 ± 0.1	1.7 ± 0.1	1.4	60	790
F	05 25 02.69	−69 38 35.8	2.79 ± 0.16	263.4 ± 0.1	1.7 ± 0.1	1.8	130	930
G	05 25 05.23	−69 38 51.2	1.39 ± 0.12	264.7 ± 0.1	2.1 ± 0.2	1.2	40	820
H	05 25 08.58	−69 38 57.0	1.66 ± 0.17	265.8 ± 0.1	0.9 ± 0.1	1.4	30	370
I	05 25 01.88	−69 39 16.1	2.95 ± 0.12	266.7 ± 0.1	2.0 ± 0.1	2.1	240	990

Notes. Column (1): Cloud name. Columns (2–9): Observed physical properties of the clouds obtained by single or double Gaussian fitting with ^{12}CO(J = 1–0) emission line. Columns (2)–(3): Position of the clouds. Column (4): Maximum radiation temperature. Column (5): Central velocity of CO spectra. Column (6): FWHM line width of CO spectra ΔV. Column (7): Diameter of clouds defined as $(S/\pi)^{0.5} \times 2$, where S is the surface area of clouds surrounded by contours of the half-level of maximum integrated intensity. Column (8): Mass of clouds derived from equation $N(H_2)/W(CO) = 7.0 \times 10^{20}$ (K km s^{-1})$^{-1}$ cm^{-2}, where $N(H_2)$ is the column density of molecular hydrogen and W(CO) is the integrated intensity of ^{12}CO(J = 1–0) (Fukui et al. 2008). Column (9): Number density of molecular hydrogen $n(H_2)$.

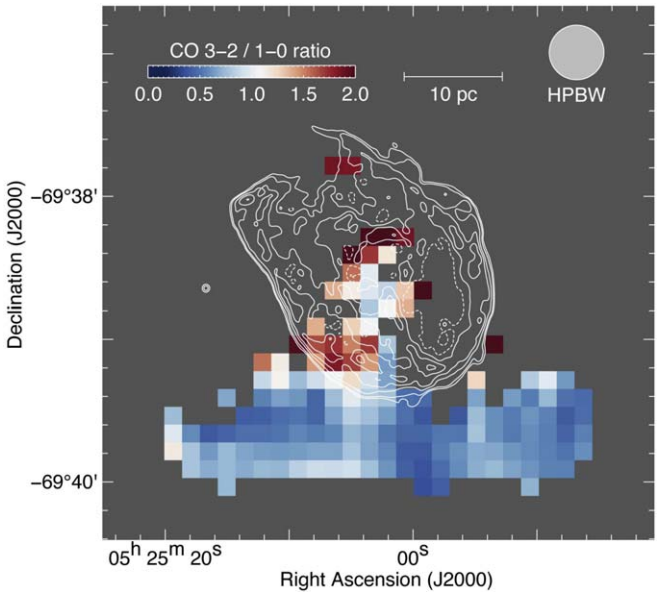

Figure 6. Intensity ratio map of ^{12}CO(J = 3–2)/^{12}CO(J = 1–0) using ASTE and ALMA. The ALMA data were smoothed to match the effective beam size of the ASTE data (an effective beam size of 23″). The beam size and scale bar are also shown in the top right corner. The velocity range is the same as in Figure 5. White dashed contours represent the X-ray intensity, whose contour levels are the same as in Figure 2(b). The gray areas represent that the ^{12}CO (J = 1–0) or ^{12}(J = 3–2) data show a low significance of ∼8σ or lower.

O, Ne, Mg, and Fe free. The Ne, Mg, and Fe abundances are significantly enhanced compared to mean local LMC values. Note that the ionization timescale for the 0.82 keV component goes to a value consistent with collisional ionization equilibrium (CIE; 3.5 × 10^{13} cm^{-3} s), while the ionization timescale for the 3.36 keV component goes to a low value of 6.6 × 10^9 cm^{-3} s, indicating that the plasma producing this emission has been shocked relatively recently. For the southwest region (the reference region), the C statistic is 1427 with 1302 DOF, and the Pearson reduced χ^2 is 1.12. The `vpshock` component is now a significant contributor (see magenta line in Figure 8(b)). The LMC absorption is now 0.0, with an upper limit of 1.3 × 10^{20} cm^{-2}. The fitted parameters for the two `vnei` components for the center and southwest regions are similar to each other; most values are within 1.0σ of each other. The major difference is the absence of the `vpshock` component in the center spectrum and the additional absorption for the center spectrum. This can be seen as the difference between the two spectra in the 0.35–1.0 keV energy range. The southwest spectrum has more emission at these lowest energies than
the center spectrum, and this emission is modeled by the `vpshock` component. This indicates that there is additional absorption along the line of sight to the center region than toward the southwest region.

4.7. Comparison with Hard X-Ray Emission

Figure 9 shows an overlay map of the 10–15 keV band image obtained with NuSTAR (colored image, Bamba et al. 2018) and the ALMA CO distribution in contours. The 10–15 keV band image represents possible synchrotron X-ray emission, although Bamba et al. (2018) could not exclude the possibility of a very high temperature plasma emission. We note that the hard X-ray emission is concentrated inside the SNR, where the molecular clouds B to G are located. Although the local intensity peaks of hard X-rays appear to be offset from the center of the molecular clouds, it is not certain whether the trend is significant because of the modest angular resolution of NuSTAR ∼18″ in HPBW (∼4.4 pc at the LMC distance). It is certain that the edge of N132D is not bright with the hard X-ray emission, which is not typical for young SNRs with synchrotron X-rays (Bamba et al. 2005).

5. Discussion

5.1. Molecular Clouds Associated with N132D

In addition to the previously known GMC, which we refer to as N132D GMC-south, we identified eight new molecular clouds toward the center and southern edge of N132D. To better understand the relationship among the clouds, high-energy radiation, and O-rich ejecta in N132D, it is essential to know which clouds are physically associated with the SNR. Here, we argue that the eight new molecular clouds resolved by ALMA are likely interacting with shock waves and lie inside a wind-blown bubble.

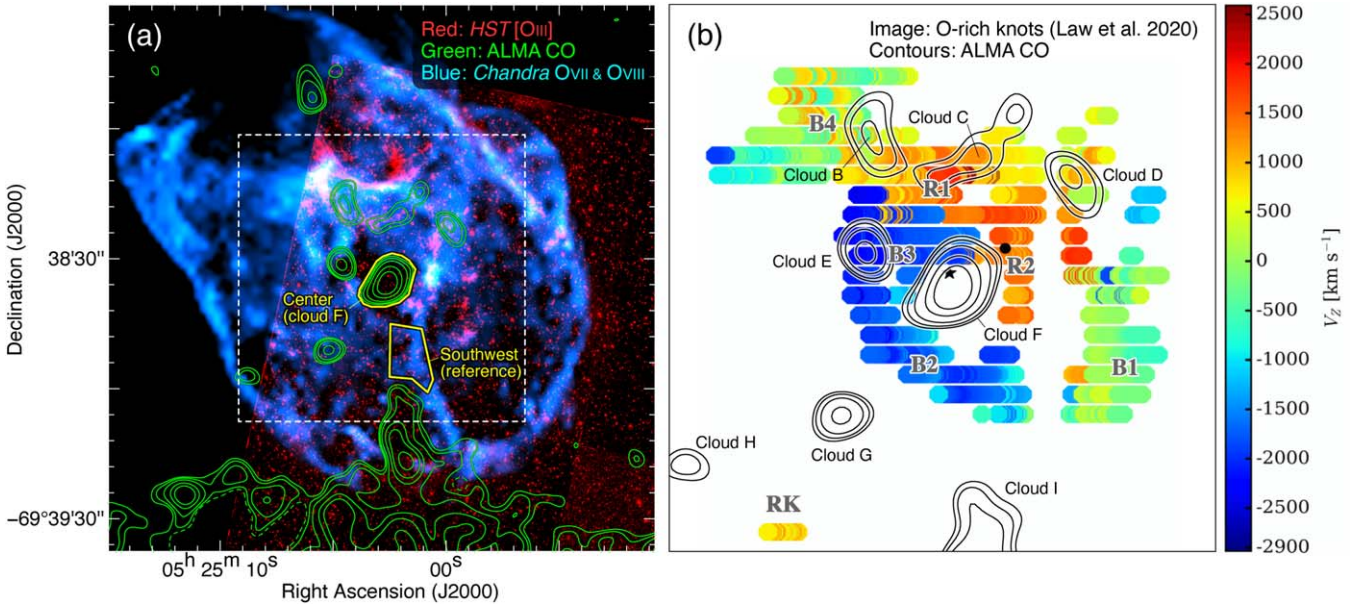

Figure 7. (a) RGB image of N132D obtained with the *HST* [O III] (red), ALMA ^{12}CO($J = 1$–0) (green contours), and Chandra O VIII emission produced using a novel method for source separation (blue, see the Appendix and Figure 11). The integration velocity range and contour levels of CO are the same as in Figure 5. Regions enclosed by solid yellow lines are used for the X-ray spectral analysis (see Section 4.6). The dashed white box represents the area shown in Figure 7(b). (b) Radial velocity distributions of O-rich knots presented by Law et al. (2020). Superposed contours indicate the ALMA ^{12}CO($J = 1$–0), whose contour levels are the same as in Figure 5. The star and filled circle represent the center of the O-rich knots and that of the X-ray shell. Major knots—B1, B2, B3, B4, R1, R2, and RK (runaway knot)—from Morse et al. (1995) are also indicated.

We first claim that the high intensity ratio of $R_{3\text{-}2/1\text{-}0} >$ 1.5–2.0 as shown in Figure 6 provides strong evidence for shock–cloud interaction. The ratio of $R_{3\text{-}2/1\text{-}0}$ is useful for measuring the degree of rotational excitation of CO molecules, because the upper state of $J = 3$ lies at 33.2 K from the ground state of $J = 0$, corresponding to ∼28 K above the state of $J = 1$ at 5.5 K. The higher ratio of $R_{3\text{-}2/1\text{-}0}$ can trace warm molecular clouds heated by shock interactions not only for the Galactic SNRs (e.g., W28, Arikawa et al. 1999; Kesteven 79, Kuriki et al. 2018), but also for the Magellanic SNRs (e.g., LMC SNR N49, Yamane et al. 2018; SMC SNR RX J0046.5 −7308, Sano et al. 2019b, 2019b). It is noteworthy that preshocked gas in N132D GMC-south shows a significantly lower intensity of $R_{3\text{-}2/1\text{-}0} \sim 0.4$, which is a typical ratio of a quiescent cloud in the LMC without external heating (e.g., Celis Peña et al. 2019).

We argue that cloud F has been completely engulfed by shocks and is located on the near side of the remnant. Figure 10 shows an enlarged view of the X-ray three-color image superposed on boundaries of molecular clouds. We find an X-ray filament toward cloud F. The color changes from red/yellow to green as one moves from east to west onto the cloud. This indicates that low-energy X-rays are suppressed toward cloud F by absorption. In fact, the LMC absorption $N_{\rm H,LMC}$ of cloud F (1.04×10^{21} cm^{-2}) is significantly higher than that of the reference region without dense clouds ($\lesssim 0.13 \times 10^{21}$ cm^{-2}). In this case, the forward shock likely propagated from behind cloud F to in front of it. Then, the X-ray filament was formed behind cloud F via shock interaction. This interpretation is also consistent with the absence of the `vpshock` component. If the shock wave is in the process of wrapping around the cloud, the thermal emission from the forward shock would be suppressed on the near side of the cloud as the shock re-forms on that side of the cloud. In addition, any thermal emission from the forward shock on the far side of the remnant is absorbed by the cloud. Both effects lead to a reduction in the thermal emission located along the line of sight to the center of the cloud.

The fitted LMC absorption $N_{\rm H,LMC}$ of $\sim 1 \times 10^{21}$ cm^{-2} toward cloud F also suggests that the molecular cloud is engulfed by shock waves. By using Equation (2), we can derive an average proton column density of cloud F to be $\sim 5 \times 10^{21}$ cm^{-2}, which is five times higher than the X-ray-derived value (see Section 4.6 and Table 3). This suggests that some of the X-ray emission originates in front of the cloud and not just behind it. The evaporating cloud scenario described in Cowie & McKee (1977) and White & Long (1991) and further explored by Zhang & Chevalier (2019) can produce such a morphology. A similar discussion is also applicable for cloud I in the southern edge of the SNR. According to Sharda et al. (2020), the LMC absorption $N_{\rm H,LMC}$ toward cloud I is ∼2–3 $\times 10^{21}$ cm^{-2}, two times lower than the average proton column density of cloud I. Although cloud I is located on the shell boundary of the SNR, it is likely that the shock is interacting with this cloud.

Additionally, the large $n_{\rm e}t$ value of the CIE plasma in cloud F is possibly consistent with a long elapsed time since the cloud was heated. Our ALMA observations revealed the molecular hydrogen density of cloud F to be 930 cm^{-3}. Considering the postshocked gas density equals one-quarter of the preshock gas density in the limit of large Mach number (see Rankin-Hugoniot shock jump conditions), the electron density toward the region can be derived to ∼560 cm^{-3} assuming the electron-to-proton density ratio of 1.2. We then obtain the ionization time of $\gtrsim$2000 yr, which is roughly consistent with the latest estimation of the SNR age of 2450 ± 195 yr (Law et al. 2020). We therefore propose a possible scenario that cloud F is completely engulfed by shocks soon after the supernova explosion.

We also argue that the molecular clouds we observe through ALMA were left behind inside a wind-blown bubble. According to Inoue et al. (2012), the surrounding ISM of a high-mass progenitor shows a highly inhomogeneous density

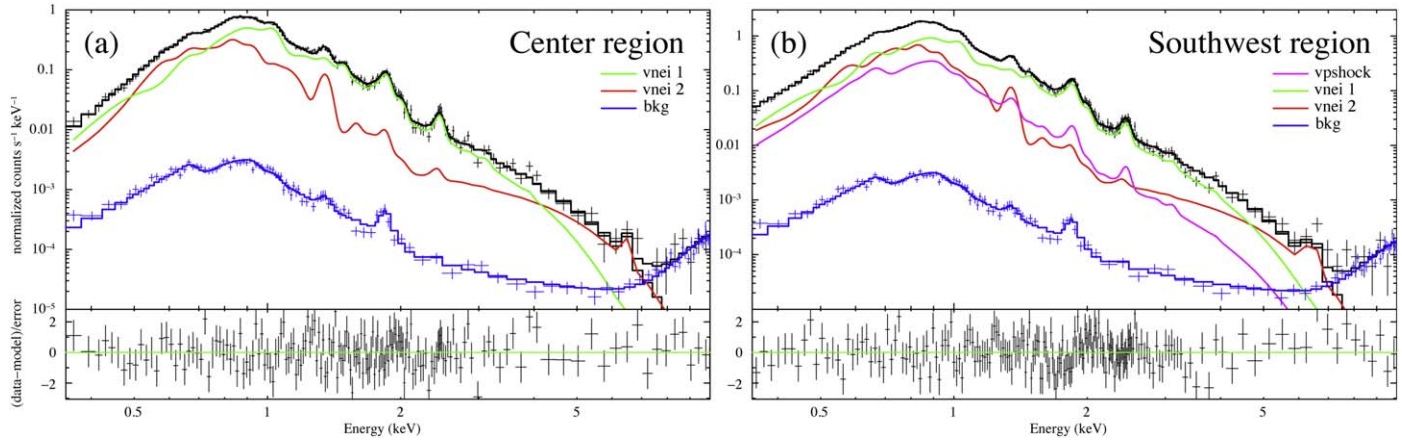

Figure 8. (a) ACIS-S spectra of the center (cloud F) and southwest (reference), with the best-fit models shown in the top panels. The magenta, green, red, and blue lines represent `vpshock`, `vnei 1`, `vnei 2`, and background components, respectively. The black lines represent the sum of the components. The bottom panels in each figure indicate (data − model)/error.

Table 3
Best-fit X-Ray Spectral Parameters

	Parameter	Center	Southwest
$N_{\rm H}$	$N_{\rm H,\ LMC}$ (10^{21} cm^{-2})	$1.04^{+0.18}_{-0.11}$	$\leqslant 0.13$
	$N_{\rm H,\ MW}$ (10^{21} cm^{-2})	1.47 (fixed)	1.47 (fixed)
vnei 1	kT_e (keV)	$0.82^{+0.03}_{-0.02}$	$0.79^{+0.04}_{-0.02}$
	$Z_{\rm O}$ (solar)	$1.18^{+0.33}_{-0.48}$	$1.92^{+0.29}_{-0.50}$
	$Z_{\rm Ne}$ (solar)	$2.36^{+0.25}_{-0.27}$	$1.88^{+0.16}_{-0.25}$
	$Z_{\rm Mg}$ (solar)	$0.94^{+0.11}_{-0.13}$	$0.70^{+0.12}_{-0.10}$
	$Z_{\rm Si}$ (solar)	$0.86^{+0.08}_{-0.10}$	$0.80^{+0.07}_{-0.09}$
	$Z_{\rm S}$ (solar)	$0.70^{+0.11}_{-0.12}$	$0.65^{+0.06}_{-0.06}$
	$Z_{\rm Fe}$ (solar)	$0.30^{+0.04}_{-0.05}$	$0.28^{+0.05}_{-0.07}$
	$n_e t$ (10^{13} cm^{-3} s)	$\geqslant 3.50$	$\geqslant 3.50$
	norm (10^{-2} cm^{-5})	$8.27^{+0.68}_{-0.76}$	$13.17^{+1.12}_{-1.82}$
vnei 2	kT_e (keV)	$3.36^{+0.47}_{-0.46}$	$2.44^{+0.49}_{-0.33}$
	$Z_{\rm O}$ (solar)	$0.87^{+0.33}_{-0.18}$	$0.64^{+0.22}_{-0.14}$
	$Z_{\rm Ne}$ (solar)	$1.38^{+0.25}_{-0.30}$	$1.70^{+0.36}_{-0.61}$
	$Z_{\rm Mg}$ (solar)	$2.05^{+0.51}_{-0.20}$	$2.58^{+0.79}_{-0.62}$
	$Z_{\rm Fe}$ (solar)	$2.36^{+1.21}_{-0.47}$	$6.38^{+4.43}_{-1.94}$
	$n_e t$ (10^{10} cm^{-3} s)	$0.66^{+0.06}_{-0.06}$	$0.47^{+0.01}_{-0.03}$
	norm (10^{-3} cm^{-5})	$4.65^{+1.16}_{-2.58}$	$6.64^{+2.40}_{-2.47}$
vpshock	kT_e (keV)	0.86 (fixed)	0.86 (fixed)
	$n_e t$ (10^{11} cm^{-3} s)	1.94 (fixed)	1.94 (fixed)
	norm (10^{-2} cm^{-5})	0.0	$3.03^{+0.02}_{-0.02}$
	cstat (d.o.f.)	1350 (1302)	1427 (1302)
	Pearson-χ^2 (reduced)	1287 (0.99)	1460 (1.12)

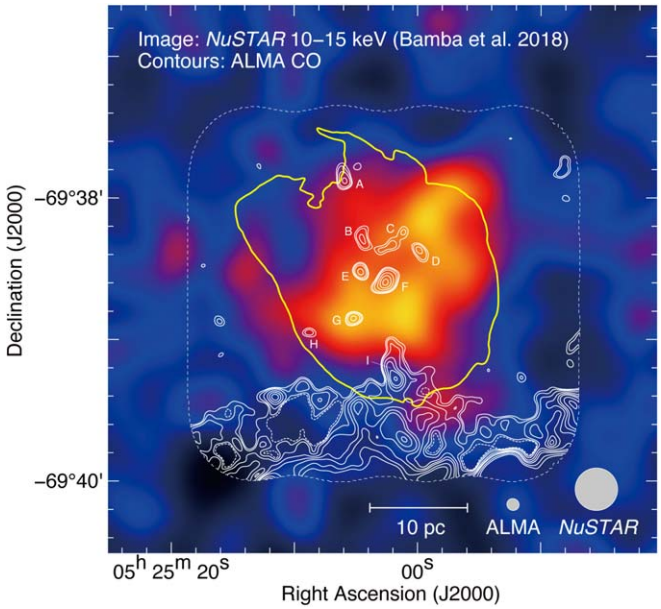

Figure 9. Map of hard X-ray emission (E: 10–15 keV) obtained with NuSTAR (Bamba et al. 2018). The white and yellow contours indicate the ALMA ^{12}CO ($J = 1$–0) and the boundary of the X-ray shell. The contour levels and integration velocity range of CO are the same as in Figure 5. The beam size and scale bar are also shown in the bottom right corner of the panel. The CO clouds A to I are also indicated.

distribution. The less dense gas such as H I clouds can be completely disrupted by the strong stellar winds, while the more dense gas such as molecular clouds can survive. As a result, a wind-blown bubble with a density of ~ 0.01 cm^{-3} coexists with dense molecular clouds with density more than $\sim 10^3$ cm^{-3}. For N132D, the wind cavity and dense clouds are seen in Figures 2(c) and 3. The H I cloud shows a cavity-like distribution in both the spatial and velocity planes. The expansion velocity of ~ 6 km s^{-1} is consistent with the typical gas motion seen in other core-collapse SNRs (e.g., Fukui et al. 2012; Kuriki et al. 2018; Sano et al. 2019b). We note that the wind-bubble explosion scenario is also proposed by previous optical and X-ray studies of N132D (Hughes 1987; Sutherland & Dopita 1995; Blair et al. 2000; Sharda et al. 2020) and modeled by Chen et al. (2003). Additionally, the estimated progenitor mass for N132D from the model of Chen et al. (2013) for an SNR evolving in a cavity is in good agreement with that from nucleosynthesis modeling of ejecta-rich regions (Sharda et al. 2020).

We emphasize that although the shock–cloud interaction has occurred, most of the dense molecular clouds can survive the shock erosion. When shock waves hit the dense clouds, the penetrating velocity can be described as $V_{\rm sh}/\sqrt{(n/n_0)}$, where $V_{\rm sh}$ is the shock velocity before collision, n_0 is the ambient density inside the wind bubble ($n_0 \sim 0.01$ cm^{-3}), and n is the number density of the molecular cloud ($n \sim 930$ cm^{-3} for the case of cloud F). Therefore, the shock waves in cloud F will be much decelerated to $1/300$ $V_{\rm sh}$, and hence the shock cannot penetrate

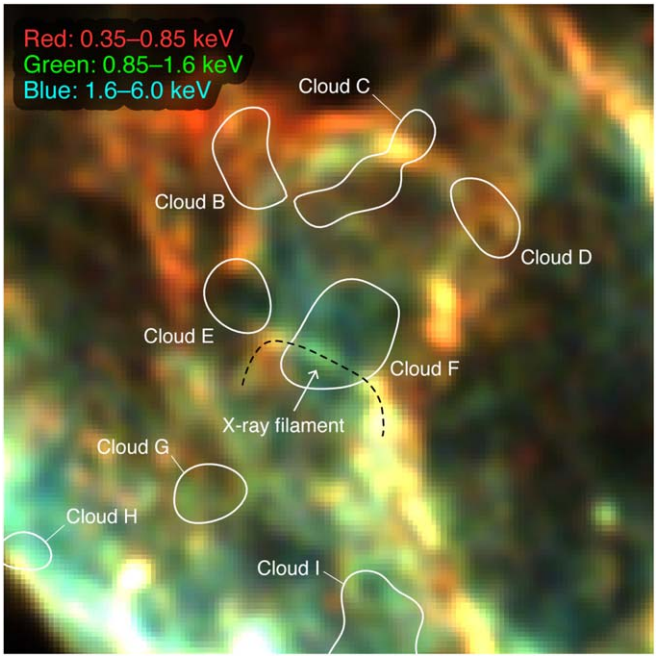

Figure 10. RGB X-ray image toward the center of N132D. The red, green, and blue colors represent the energy bands 0.35–0.85 keV, 0.85–1.6 keV, and 1.6–6.0 keV, respectively. Superposed contours indicate boundaries of ALMA CO clouds B to I as shown in Figure 5, whose contour levels are 1.2 K km s^{-1}. Note that cloud A is located outside the field of view. The dashed line indicates the X-ray filament, discussed in Section 5.1.

into the cloud within a few thousand years. The numerical results also support this idea (e.g., Celli et al. 2019). Furthermore, evaporation of the shocked cloud is also negligible, due to the small thermal capacity of the SNR's shocks. Tatematsu et al. (1990) and Sasaki et al. (2006) discovered shocked molecular clouds in the middle-aged Galactic SNR G109.1−1.0 with the age of $\sim 1.4 \times 10^4$ yr (Sasaki et al. 2013), which survived the encounter. The surviving clouds, with a total mass of 63 $M_\odot$, are associated with a thermal X-ray lobe. The authors conclude that the X-ray lobe was likely formed by the evaporation of a small outer portion of the clouds; the mass ratio of the thermal plasma relative to the molecular clouds is less than 10% (Sasaki et al. 2006). This interpretation is also supported by numerical simulations (Bolte et al. 2015). For N132D, clouds B to F have been partially evaporated because the bright Hα emission and thermal X-rays are seen in their vicinity (see Figures 2 and 5). In other words, almost all parts of the clouds in N132D likely survived shock erosion or evaporation, considering the large total cloud mass of $\sim$750 $M_\odot$ and young age of N132D ($\sim$2500 yr). Therefore, N132D may be considered to represent an early stage of the mixed-morphology SNR (e.g., Rho & Petre 1998).

The hard X-ray enhancements around the shocked clouds also provide alternative evidence for an inhomogeneous density distribution of the ISM. When a supernova shock wave propagates into an inhomogeneous ISM with a density fluctuation of roughly 10^5, the shock–cloud interaction may generate turbulence that enhances the magnetic field up to $\sim$1 mG at the surface of the shocked clouds (e.g., Inoue et al. 2009, 2012). This can be observed as synchrotron X-rays or a radio continuum enhancement around the shocked gas clouds (e.g., Sano et al. 2010, 2013, 2015a, 2017b, 2017a; Yamane et al. 2018; Okuno et al. 2018). On the other hand, the shock–cloud interaction will develop multiple reflected shock structures that can heat the gas up to high temperatures (e.g., Sano et al. 2019a). For N132D, the observational trend in Figure 9—a spatial correspondence between the 10–15 keV X-rays and molecular clouds B to F—shows possible evidence for the shock–cloud interaction with the magnetic field amplification or shock ionization. To confirm this idea, we need conclusive evidence of a synchrotron X-ray or high-temperature plasma enhancement around the molecular clouds with sufficient angular resolution. A deep exposure with Chandra offers the possibility of extracting the hard X-ray spectral component spatially coincident with the molecular clouds.

In conclusion, the eight new molecular clouds presented here are possibly located inside the wind-blown bubble formed by stellar winds from the progenitor of N132D, and these clouds are likely engulfed by supernova shock waves. On the other hand, the relationship between these clouds and the O-rich ejecta is still unknown from the current data set (see Section 4.5 and Figure 7). It is possible that the O-rich emission of optical and X-rays was efficiently produced by reverse shocks because of the shock interaction with the dense molecular clouds (e.g., Milisavljevic & Fesen 2015). Future ALMA observations with $\sim$0.1 pc resolution will allow us to compare spatial and kinematic distributions of the ISM/circumstellar medium (CSM) and ejecta.

5.2. Is N132D the Energetic Accelerator of Cosmic-Ray Protons?

N132D is thought to be a promising candidate for a hadronic gamma-ray emitter because of its bright teraelectronvolt gamma rays and very weak or absent synchrotron X-ray emission (Bamba et al. 2018). Although a detailed spatial comparison between the CO data and the gamma-ray emission could not be carried out, the presence of shocked molecular clouds provides support for the hadronic origin of gamma rays in N132D. Assuming that this hypothesis is correct, we derive the total energy of accelerated cosmic-ray protons, $W_{\rm p}$, in N132D while taking into account the target gas density. Previous studies measured the values of $W_{\rm p} \sim 10^{50}$–10^{51} erg using the X-ray-based or model-dependent gas density (H.E.S.S. Collaboration et al. 2015; Bamba et al. 2018). Here, we reconsider the total energy of cosmic-ray protons in N132D using the neutral gas density, which is derived from radio observations.

It should be emphasized that teraelectronvolt gamma rays are emitted from the direction of N132D itself, rather than from the surrounding GMCs or H I cloud, even after taking into consideration the PSF of the gamma-ray image (Figure 1). This implies that the surrounding three to four GMCs and the southern H I cloud do not significantly contribute to the gamma-ray emission via the hadronic process.[19] In the present study, we therefore focus on the target gas density within the shell of the SNR.

We estimate the target proton density within a wind-blown bubble. As discussed in Section 5.1, the molecular clouds are located inside the wind bubble. Since the intercloud density in the bubble is thought to be significantly low ($\sim$0.01 cm^{-3}, e.g.,

[19] Note that future gamma-ray observatories with high angular resolution and high sensitivity have the potential to detect gamma rays from the escaped cosmic-ray protons from the surrounding GMCs and H I cloud. The Cerenkov Telescope Array (CTA) can test the presence of high-energy particles escaped from N132D.

Weaver et al. 1977), the only plausible mechanism to produce gamma-ray emission concentrated in the center of the SNR is if the cosmic-ray protons interact with the molecular clouds. According to H.E.S.S. Collaboration et al. (2015), the total energy of cosmic-ray protons W_p can be described in the case of the hadron-dominant model as

$$W_p \sim 10^{52}(n_H/1\ \mathrm{cm}^{-3})^{-1}\ (\mathrm{erg}), \quad (3)$$

where n_H is the number density of interstellar protons. Adopting proton densities of molecular clouds of 260–1980 cm^{-3} (see Table 2), we then obtain $W_p \sim 0.5$–3.8×10^{49} erg. This is comparable to the values obtained for the Galactic gamma-ray SNRs ($\sim 10^{48}$–10^{49} erg; e.g., Fukui et al. 2012, 2017; Yoshiike et al. 2013; Fukuda et al. 2014; Kuriki et al. 2018; Sano et al. 2019c). Note that the derived value gives a conservative lower limit on the total energy of cosmic-ray protons, because the hadronic gamma-ray emission can be observed only toward the gas cloud even if cosmic-ray protons have an azimuthally isotropic distribution. In other words, there are cosmic-ray protons that do not interact with the molecular clouds and do not produce gamma rays, and the value of W_p should be slightly increased. In any case, N132D can be classified as a common accelerator of cosmic-ray protons in the Local Group of galaxies.

We also discuss an alternative case that the shock front of N132D has reached the cavity wall of the wind-blown bubble. In this case, atomic hydrogen gas within the wind shell acts as the target for cosmic-ray protons. The column density of atomic hydrogen $N_p(\mathrm{H\,I})$ is calculated using the following equation (Dickey & Lockman 1990):

$$N_p(\mathrm{H\,I}) = 1.823 \times 10^{18} \cdot W(\mathrm{H\,I})\ (\mathrm{cm}^{-2}), \quad (4)$$

where W(H I) is the integrated intensity of H I in units of K km s^{-1}. Since W(H I) toward N132D has a large uncertainty because of the radio continuum absorption (see Figures 3 and 4), we derive it by referring to the H I intensity surrounding the shell. The typical value of W(H I) near the shell is $\sim$500 K km s^{-1} (see Figure 2(c)), and hence the average column density of atomic hydrogen is derived as $\sim 0.9 \times 10^{21}\ \mathrm{cm}^{-2}$. Considering the wind-bubble expansion, the atomic hydrogen gas was swept up within the thick wind shell. We here assume that the diameter and thickness of the H I wind shell are $\sim$25 pc and $\sim$5 pc, respectively. The former corresponds to an effective diameter of N132D, and the latter represents the typical thickness of a wind shell surrounding a high-mass star or core-collapse SNR (e.g., Yamamoto et al. 2006; Fukui et al. 2012, 2017; Sano et al. 2019c). We finally obtain the atomic hydrogen density within the wind shell to be $\sim 30\ \mathrm{cm}^{-3}$, corresponding to $W_p \sim 3 \times 10^{50}$ erg. This energy is significantly higher than the values that are seen in Galactic gamma-ray SNRs, and hence N132D might be an energetic accelerator of cosmic-ray protons, as mentioned before (H.E.S.S. Collaboration et al. 2015; Bamba et al. 2018). To confirm the shock interaction with the wind shell, further H I observations are needed. The Australian Square Kilometre Array Pathfinder (ASKAP), MeerKAT, and the Square Kilometre Array (SKA) will be able to spatially resolve the wind-blown bubble of H I with fine angular resolution and high sensitivity.

6. Conclusions

We have presented new ^{12}CO(J = 1–0, 3–2) observations toward the LMC SNR N132D using ALMA and ASTE. The primary conclusions are summarized as follows:

1. We have revealed the presence of diffuse CO emission inside the X-ray shell in addition to the previously known GMC at the southern edge of N132D. ALMA observations spatially resolved the diffuse CO emission into nine molecular clouds, whose sizes and masses are 1.2–2.2 pc and 30–240 $M_\odot$. High intensity ratios of CO J = 3–2/1–0 $>$ 1.5 are seen toward the molecular clouds, indicating that shock heating has occurred. The expansion H I shell with an expanding velocity of $\sim$6 km s^{-1} is also found toward N132D.
2. Spatially resolved X-ray spectroscopy has revealed that the emission from the line of sight to cloud F can be well represented by a model with absorption in excess of the LMC absorption of $N_H = 1.04 \times 10^{21}\ \mathrm{cm}^{-2}$ and two NEI thermal components (one of which approaches CIE conditions) and no thermal component for the forward-shock emission. On the other hand, the fit to the X-ray spectrum of an adjacent region off of cloud F shows no additional absorption compared to the LMC value and requires a thermal component for the forward shock in addition to the two NEI components. The larger absorption and the absence of a thermal component associated with the forward shock along the line of sight to cloud F suggest that cloud F has been engulfed by shocks and is located on the near side of remnant.
3. We propose that the molecular clouds existed in the wind-blown bubble of the progenitor before the SNe explosion. The large $n_e t$ value of one component of the plasma along the line of sight to cloud F is consistent with an elapsed time of $\gtrsim$2000 yr since the cloud was heated. The inhomogeneous density distribution inside the bubble—diffuse gas of $\sim 0.01\ \mathrm{cm}^{-3}$ and dense clouds of $\sim 1000\ \mathrm{cm}^{-3}$—is also consistent with synchrotron X-ray or high-temperature plasma enhancement around the shocked clouds through magnetic field amplification or shock ionization.
4. If the hadronic process is the dominant contributor to the gamma-ray emission, the shock-engulfed molecular clouds play a role as targets for cosmic rays. We estimate the total energy of cosmic-ray protons accelerated in N132D to be $\sim$0.5–3.8×10^{49} erg as a conservative lower limit, which is roughly the same value as seen in Galactic gamma-ray SNRs. The total energy could be as high as $\sim 3 \times 10^{50}$ erg if the shock front has reached the edge of the wind-blown cavity and the wind shell of H I has become a primary target for cosmic-ray protons. If the latter case is correct, N132D might be a very energetic accelerator of cosmic rays in the Local Group of galaxies.

This paper makes use of the following ALMA data: ADS/JAO.ALMA#2013.1.01042.S. ALMA is a partnership of ESO (representing its member states), NSF (USA), and NINS (Japan), together with NRC (Canada), MOST and ASIAA (Taiwan), and KASI (Republic of Korea), in cooperation with the Republic of Chile. The Joint ALMA Observatory is operated by ESO, AUI/NRAO, and NAOJ. The ASTE radio telescope is operated by NAOJ. The Mopra radio telescope is part of the Australia

telescope and is funded by the Commonwealth of Australia for operation as a National Facility managed by the CSIRO. The University of New South Wales Mopra Spectrometer Digital Filter Bank used for these Mopra observations was provided with support from the Australian Research Council, together with the University of New South Wales, the University of Adelaide, University of Sydney, Monash University, and the CSIRO. The scientific results reported in this article are based on data obtained from the Chandra Data Archive (Obs IDs: 5532, 7259, and 7266). This research has made use of software provided by the Chandra X-ray Center (CXC) in the application package CIAO (v4.12). This work is based on observations made with the NASA/ESA Hubble Space Telescope and obtained from the Hubble Legacy Archive, which is a collaboration between the Space Telescope Science Institute (STScI/NASA), the Space Telescope European Coordinating Facility (ST-ECF/ESA), and the Canadian Astronomy Data Centre (CADC/NRC/CSA). This research made use of the SAO/NASA Astrophysics Data System (ADS) bibliographic services. This work was supported by JSPS KAKENHI grant Nos. JP16K17664 (H.S.), JP19K14758 (H.S.), JP19H05075 (H.S.), and JP19K03908 (A.B.). H.S. is also supported by the ALMA Japan Research Grant of NAOJ Chile Observatory (grant No. NAOJ-ALMA-244). This work is supported in part by a Shiseido Female Researcher Science Grant (A.B.). P.S. is supported by the Australian Government Research Training Program (AGRTP) Scholarship. C.L. acknowledges funding from the National Science Foundation Graduate Research Fellowship under grant DGE1745303. K.T. was supported by NAOJ ALMA Scientific Research grant No. 2016-03B. M.S. acknowledges support by the Deutsche Forschungsgemeinschaft through the Heisenberg professor grants SA 2131/5-1 and 12-1. We are also grateful to the anonymous referee for useful comments which helped the authors to improve the paper.

Software: CASA (v5.4.0: McMullin et al. 2007), CIAO (v4.12: Fruscione et al. 2006), CALDB (v4.9.1: Graessle et al. 2007), Xspec (Arnaud 1996), SAO ds9 (Joye & Mandel 2003).

Appendix
X-Ray Map for Oxygen-dominated Components

Despite their multidimensional nature, X-ray data are most frequently analyzed as 2D images or 1D spectra independently, therefore disconnecting the spatial and morphological information. To generate the oxygen X-ray map presented in Figure 7(a), we used a novel deblending technique recently adapted to X-ray data in Picquenot et al. (2019) that takes full advantage of the 3D (X, Y, E) information provided by X-ray spectroimagers. This method (the generalized morphological component analysis or GMCA) was initially developed to separate the cosmic microwave background image from the foregrounds in *Planck* data (Bobin et al. 2015, 2016). The general idea is to decompose the input X-ray data cube into a linear sum of images and associated spectra, each component being different from the next one by its morphological and spectral signature. Note that the algorithm has a blind source separation approach and has no instrumental (instrument response) nor astrophysical (spectral emission) knowledge. Only the number of components to retrieve is fixed by the user. The main disentangling factor is the morphological diversity of each component in the wavelet domain[20] and their associated spectral signatures.

[20] The wavelet transform is applied to each image slice of the data cube in order to enhance the contrast between small- and large-scale features.

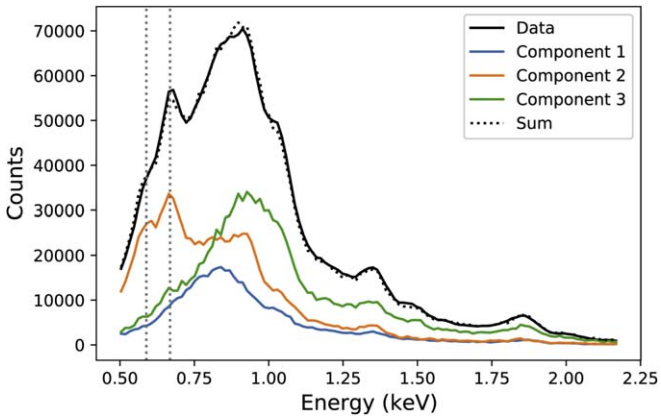

Figure 11. Spectral decomposition of the X-ray data cube into different spectral components with a novel deblending method. The positions of the O VII and O VIII lines at 0.574 and 0.654 keV, respectively, are shown by the dotted lines.

Based on the same Chandra data set as presented in Section 3.3, a data cube was produced with an instrumental energy channel binning of 14.6 eV and a spatial bin size of 1.5 arcsec. The algorithm was applied in the 0.5 to 2.2 keV band, and the number of components to retrieve was fixed to three. Figure 11 shows the resulting spectral decomposition with one component dominating the low energies and exhibiting notable line emission at 0.574, 0.654 keV (dotted lines in Figure 11). Due to this spectral feature and the morphological similarities to the *HST* [O III] map (see Figure 7(a)), we associate this component with an oxygen-rich component. The image associated with this spectral component is shown in Figure 7(a) (blue). As this component is dominating the 0.5–0.8 keV band, it is the most sensitive to absorption along the line of sight, and the drops in flux in the image reflect the regions of highest absorption traced by the ALMA CO data.

ORCID iDs

H. Sano https://orcid.org/0000-0003-2062-5692
P. P. Plucinsky https://orcid.org/0000-0003-1415-5823
A. Bamba https://orcid.org/0000-0003-0890-4920
P. Sharda https://orcid.org/0000-0003-3347-7094
M. D. Filipović https://orcid.org/0000-0002-4990-9288
C. J. Law https://orcid.org/0000-0003-1413-1776
R. Z. E. Alsaberi https://orcid.org/0000-0001-5609-7372
Y. Yamane https://orcid.org/0000-0001-8296-7482
K. Tokuda https://orcid.org/0000-0002-2062-1600
F. Acero https://orcid.org/0000-0002-6606-2816
M. Sasaki https://orcid.org/0000-0001-5302-1866
J. Vink https://orcid.org/0000-0002-4708-4219
S. Inutsuka https://orcid.org/0000-0003-4366-6518
J. Shimoda https://orcid.org/0000-0003-3383-2279
K. Tsuge https://orcid.org/0000-0002-2794-4840
N. Maxted https://orcid.org/0000-0003-2762-8378
G. Rowell https://orcid.org/0000-0002-9516-1581
T. Onishi https://orcid.org/0000-0001-7826-3837
A. Kawamura https://orcid.org/0000-0001-7813-0380
K. Tachihara https://orcid.org/0000-0002-1411-5410

References

Acero, F., Ackermann, M., Ajello, M., et al. 2016, ApJS, 224, 8
Ackermann, M., Albert, A., Atwood, W. B., et al. 2016, A&A, 586, A71
Arikawa, Y., Tatematsu, K., Sekimoto, Y., et al. 1999, PASJ, 51, L7

Arnaud, K. A. 1996, in ASP Conf. Ser. 101, Astronomical Data Analysis Software and Systems V, ed. G. H. Jacoby & J. Barnes (San Francisco, CA: ASP), 17
Badenes, C., Maoz, D., & Draine, B. T. 2010, MNRAS, 407, 1301
Bamba, A., Ohira, Y., Yamazaki, R., et al. 2018, ApJ, 854, 71
Bamba, A., Yamazaki, R., Yoshida, T., et al. 2005, ApJ, 621, 793
Banas, K. R., Hughes, J. P., Bronfman, L., et al. 1997, ApJ, 480, 607
Bell, A. R. 1978, MNRAS, 182, 147
Blair, W. P., Morse, J. A., Raymond, J. C., et al. 2000, ApJ, 537, 667
Blandford, R. D., & Ostriker, J. P. 1978, ApJL, 221, L29
Bobin, J., Rapin, J., Larue, A., et al. 2015, ITSP, 63, 1199
Bobin, J., Sureau, F., & Starck, J.-L. 2016, A&A, 591, A50
Bolte, J., Sasaki, M., & Breitschwerdt, D. 2015, A&A, 582, A47
Borkowski, K. J., Hendrick, S. P., & Reynolds, S. P. 2007, ApJL, 671, L45
Borkowski, K. J., Lyerly, W. J., & Reynolds, S. P. 2001, ApJ, 548, 820
Bozzetto, L. M., Filipović, M. D., Vukotić, B., et al. 2017, ApJS, 230, 2
Bykov, A. M., Ellison, D. C., Marcowith, A., & Osipov, S. M. 2018, SSRv, 214, 41
Cash, W. 1979, ApJ, 228, 939
Celis Peña, M., Paron, S., Rubio, M., et al. 2019, A&A, 628, A96
Celli, S., Morlino, G., Gabici, S., et al. 2019, MNRAS, 487, 3199
Chen, Y., Zhang, F., Williams, R. M., et al. 2003, ApJ, 595, 227
Chen, Y., Zhou, P., & Chu, Y.-H. 2013, ApJL, 769, L16
Cornwell, T. J. 2008, ISTSP, 2, 793
Cowie, L. L., & McKee, C. F. 1977, ApJ, 211, 135
Danziger, I. J., & Dennefeld, M. 1976, PASP, 88, 44
Dermer, C. D. 1986, A&A, 157, 223
Desai, K. M., Chu, Y.-H., Gruendl, R. A., et al. 2010, AJ, 140, 584
Dickel, J. R., & Milne, D. K. 1995, AJ, 109, 200
Dickey, J. M., & Lockman, F. J. 1990, ARA&A, 28, 215
Dopita, M. A., Vogt, F. P. A., Sutherland, R. S., et al. 2018, ApJS, 237, 10
Ezawa, H., Kawabe, R., Kohno, K., et al. 2004, Proc. SPIE, 5489, 763
Fazio, G. G. 1967, ARA&A, 5, 481
Foster, A. R., Ji, L., Yamaguchi, H., Smith, R. K., & Brickhouse, N. S. 2013, in AIP Conf. Ser. 1545 (Melville, NY: AIP), 252
France, K., Beasley, M., Keeney, B. A., et al. 2009, ApJL, 707, L27
Fruscione, A., McDowell, J. C., Allen, G. E., et al. 2006, Proc. SPIE, 6270, 62701V
Fukuda, T., Yoshiike, S., Sano, H., et al. 2014, ApJ, 788, 94
Fukui, Y., Kawamura, A., Minamidani, T., et al. 2008, ApJS, 178, 56
Fukui, Y., Sano, H., Sato, J., et al. 2012, ApJ, 746, 82
Fukui, Y., Sano, H., Sato, J., et al. 2017, ApJ, 850, 71
Funk, S. 2015, ARNPS, 65, 245
Graessle, D. E., Evans, I. N., Glotfelty, K., et al. 2007, ChNew, 14, 33
H.E.S.S. Collaboration, Abdalla, H., Abramowski, A., et al. 2018a, A&A, 612, A6
H.E.S.S. Collaboration, Abdalla, H., Abramowski, A., et al. 2018b, A&A, 612, A7
H.E.S.S. Collaboration, Abramowski, A., Aharonian, F., et al. 2015, Sci, 347, 406
H.E.S.S. Collaboration, Abramowski, A., Aharonian, F., et al. 2018c, A&A, 612, A4
HI4PI Collaboration, ben Bekhti, N., Floer, L., et al. 2016, A&A, 594A, 116
Hughes, J. P. 1987, ApJ, 314, 103
Hughes, J. P., Hayashi, I., & Koyama, K. 1998, ApJ, 505, 732
Inoue, H., Muraoka, K., Sakai, T., et al. 2008, in Proc. Ninteenth Int. Symp. on Space Terahertz Technology (Groningen: Univ. Groningen Press), 281, https://www.nrao.edu/meetings/isstt/papers/2008/2008281285.pdf
Inoue, T., Yamazaki, R., & Inutsuka, S.-I. 2009, ApJ, 695, 825
Inoue, T., Yamazaki, R., Inutsuka, S.-i., & Fukui, Y. 2012, ApJ, 744, 71
Joye, W. A., & Mandel, E. 2003, in ASP Conf. Ser. 295, Astronomical Data Analysis Software and Systems XII, ed. H. E. Payne, R. I. Jedrzejewski, & R. N. Hook (San Francisco, CA: ASP), 489
Kaastra, J. S. 2017, A&A, 605, A51
Kim, S., Staveley-Smith, L., Dopita, M. A., et al. 2003, ApJS, 148, 473
Kuriki, M., Sano, H., Kuno, N., et al. 2018, ApJ, 864, 161
Lasker, B. M. 1978, ApJ, 223, 109
Lasker, B. M. 1980, ApJ, 237, 765
Law, C. J., Milisavljevic, D., Patnaude, D. J., et al. 2020, ApJ, 894, 73
Leahy, D., Wang, Y., Lawton, B., Ranasinghe, S., & Filipović, M. 2019, AJ, 158, 149
Maggi, P., Haberl, F., Kavanagh, P. J., et al. 2016, A&A, 585, A162
Martin, P., Lu, C.-C., Voelk, H., Renaud, M., & Filipovic, M. 2019, in Cherenkov Telescope Array Consortium, ed. B. S. Acharya et al. (Singapore: World Scientific Publishing), 125
McMullin, J. P., Waters, B., Schiebel, D., Young, W., & Golap, K. 2007, in ASP Conf. Series 376, Astronomical Data Analysis Software and Systems XVI, ed. R. A. Shaw, F. Hill, & D. J. Bell, 127
Milisavljevic, D., & Fesen, R. A. 2015, Sci, 347, 526
Minamidani, T., Tanaka, T., Mizuno, Y., et al. 2011, AJ, 141, 73
Morse, J. A., Blair, W. P., Dopita, M. A., et al. 1996, AJ, 112, 509
Morse, J. A., Winkler, P. F., & Kirshner, R. P. 1995, AJ, 109, 2104
Ohira, Y., Yamazaki, R., Kawanaka, N., et al. 2012, MNRAS, 427, 91
Okuno, T., Tanaka, T., Uchida, H., et al. 2018, PASJ, 70, 77
Picquenot, A., Acero, F., Bobin, J., et al. 2019, A&A, 627, A139
Pietrzyński, G., Graczyk, D., Gieren, W., et al. 2013, Natur, 495, 76
Rho, J., & Petre, R. 1998, ApJL, 503, L167
Sano, H., Fukuda, T., Yoshiike, S., et al. 2015a, ApJ, 799, 175
Sano, H., Fukui, Y., Yoshiike, S., et al. 2015b, in ASP Conf. Series 499, Revolution in Astronomy with ALMA: The Third Year, ed. D. Iono et al. (San Francisco, CA: ASP), 257
Sano, H., Matsumura, H., Nagaya, T., et al. 2019a, ApJ, 873, 40
Sano, H., Matsumura, H., Yamane, Y., et al. 2019b, ApJ, 881, 85
Sano, H., Reynoso, E. M., Mitsuishi, I., et al. 2017a, JHEAp, 15, 1
Sano, H., Rowell, G., Reynoso, E. M., et al. 2019c, ApJ, 876, 37
Sano, H., Sato, J., Horachi, H., et al. 2010, ApJ, 724, 59
Sano, H., Tanaka, T., Torii, K., et al. 2013, ApJ, 778, 59
Sano, H., Yamane, Y., Tokuda, K., et al. 2018, ApJ, 867, 7
Sano, H., Yamane, Y., Voisin, F., et al. 2017b, ApJ, 843, 61
Sasaki, M., Kothes, R., Plucinsky, P. P., et al. 2006, ApJL, 642, L149
Sasaki, M., Plucinsky, P. P., Gaetz, T. J., et al. 2013, A&A, 552, A45
Schenck, A., Park, S., & Post, S. 2016, AJ, 151, 161
Seok, J. Y., Koo, B.-C., & Onaka, T. 2013, ApJ, 779, 134
Sharda, P., Gaetz, T. J., Kashyap, V. L., & Plucinsky, P. P. 2020, ApJ, 894, 145
Sorai, K., Sunada, K., Okumura, S. K., et al. 2000, Proc. SPIE, 4015, 86
Stecker, F. W. 1971, Cosmic Gamma Rays NASA-SP-249
Sutherland, R. S., & Dopita, M. A. 1995, ApJ, 439, 365S
Tappe, A., Rho, J., Boersma, C., et al. 2012, ApJ, 754, 132
Tappe, A., Rho, J., & Reach, W. T. 2006, ApJ, 653, 267
Tatematsu, K., Fukui, Y., Iwata, T., et al. 1990, ApJ, 351, 157
Verner, D. A., Ferland, G. J., Korista, K. T., et al. 1996, ApJ, 465, 487
Vogt, F., & Dopita, M. A. 2011, Ap&SS, 331, 521
Weaver, R., McCray, R., Castor, J., et al. 1977, ApJ, 218, 377
White, R. L., & Long, K. S. 1991, ApJ, 373, 543
Williams, B. J., Borkowski, K. J., Reynolds, S. P., et al. 2006, ApJL, 652, L33
Wilms, J., Allen, A., & McCray, R. 2000, ApJ, 542, 914
Wong, T., Hughes, A., Ott, J., et al. 2011, ApJS, 197, 16
Xiao, X., & Chen, Y. 2008, AdSpR, 41, 416
Yamamoto, H., Kawamura, A., Tachihara, K., et al. 2006, ApJ, 642, 307
Yamane, Y., Sano, H., van Loon, J. T., et al. 2018, ApJ, 863, 55
Yoshiike, S., Fukuda, T., Sano, H., et al. 2013, ApJ, 768, 179
Zhang, D., & Chevalier, R. A. 2019, MNRAS, 482, 1602
Zhu, H., Slane, P., Raymond, J., & Tian, W. W. 2019, ApJ, 882, 135